

SERS background imaging – A versatile tool towards more reliable SERS analytics

Paul Ebersbach

Leibniz-Institut für Analytische Wissenschaften - ISAS - e.V.

Ute Münchberg

Leibniz-Institut für Analytische Wissenschaften - ISAS - e.V.

Erik Freier (✉ erik.freier@isas.de)

Leibniz-Institut für Analytische Wissenschaften - ISAS - e.V. <https://orcid.org/0000-0002-0559-4210>

Article

Keywords: Surface-enhanced Raman scattering, substrate, imaging

Posted Date: August 1st, 2020

DOI: <https://doi.org/10.21203/rs.3.rs-41355/v1>

License:   This work is licensed under a Creative Commons Attribution 4.0 International License. [Read Full License](#)

Abstract

Surface-enhanced Raman scattering (SERS) is a highly selective and sensitive straightforward analytical method, which is however not yet established in routine analysis due to a lack of reliability and reproducibility. To address this limitation, we show the distinct correlation of the ever-present but often neglected broad SERS background continuum with the SERS signal intensity of the analyte and how to exploit this correlation for an easy-to-handle, automatable and more reliable SERS measurement. First, fast and high-contrast imaging of the SERS substrate is performed for hot spot localisation utilizing the SERS background. Subsequently, highly enhanced SERS spectra are recorded at the centre of these spots. Furthermore, we correlate our SERS background imaging with other optical imaging modalities and electron microscopy to assess structure-property relationships. Monte Carlo simulations based on actual measurements illustrate the sampling error of a conventional SERS experiment and the advantages our method provides.

Introduction

The most remarkable property of surface-enhanced Raman scattering (SERS) is probably its capability to enhance the Raman effect up to the level of single molecular detection^{1,2}. Nevertheless, SERS did not yet achieve a breakthrough on the commercial market or even high impact in applied analytical research³. This is due to its challenging reproducibility and reliability, taking effect especially in highly sensitive so-called hot spot-based SERS measurements³⁻⁸.

The SERS effect is a complex process based on a three-body interaction of photons, molecules and nanostructures³. These nanostructures, in the following named SERS substrate, play a special role as they not only act as a signal amplifier but also must enable adsorption of or at least close contact to the analyte, as the enhancement decreases exponentially with distance³. Highest electromagnetic enhancement – the main contributor of the SERS effect – is only obtained in localised optical near-fields, the so-called ‘hot spots’ appearing in interparticle nanogaps (< 10 nm) formed *e.g.* in nanoparticle aggregates^{5,9}. Hot spots are responsible for the single molecule detection capabilities⁹ but also cause the enormous signal fluctuations usually observed in SERS experiments^{7,8}. The variability in hot spot-based SERS measurements is due to small morphological variations of the gaps in size, shape and distance^{4,7,8}, a nonuniform analyte distribution inside the gaps⁷ and the often heterogeneous distribution of only a few hot spots over a large area, which makes them also difficult to localise¹⁰. Furthermore, the reliability can be impaired by the photoinduced formation of signal intense amorphous carbon¹¹ often occurring in hot spots¹²⁻¹⁴. A strategy towards more reliable and reproducible SERS analytics is therefore the development of gap-free or “hot surfaces” rather than “hot spot” SERS substrates^{5,7,15}. They show better controllable properties but also often only a moderate SERS enhancement³. Applied research however requires both features. A high sensitivity is especially necessary to enable the detection of analytes with small Raman cross-sections or weakly adsorbed species. Actually, molecular generality – the detection capability of a great variety of analytes – has always been the most challenging bottleneck of SERS due to the low Raman cross sections and/or weak absorption capabilities of many analytes^{3,4}. Developing SERS substrates therefore involves the struggle to find a balance between reproducibility and sensitivity.

The development and quality control of SERS substrates also requires sophisticated analytical imaging relationship between optical properties and the

underlying nanostructure. While Scanning Electron Microscopy (SEM) provides direct access to the basic shape and size of the nanostructure, optical methods give insight into the optical properties of these structures. As the sizes of these structures are well below the optical diffraction limit (*e.g.* hot spots 1–10 nm)¹⁶, the methods are strictly separated into near and far-field optical methods. Near-field optical tip-based methods like s-SNOM-SERS¹⁷ and functionalised TERS^{18,19} or electron microscopy-based methods like PEEM¹⁹ and STEM/EELS²⁰ as well as super resolution-imaging^{16,21} enable nanoscale mapping of localised surface plasmon resonances (LSPRs)²⁰, the electromagnetic field enhancement^{17–19} or of individual Raman bands^{16,17,21} in hot spots and are important tools in fundamental research to study structural-functional relationships. Due to the high equipment expense, difficult handling and a low versatility these methods are however not common in applied analytical SERS research. Conventional SERS experiments are mostly performed with far-field optical methods, in which a sub-wavelength hot spot appears as a diffraction-limited spot. Spectral acquisition delivers average spectra of the diffraction-limited areas. The uniformity of the signal enhancement on a SERS substrate is most often checked by pointwise^{22–24} or linewise²⁵ Raman mapping or by randomly selecting different measurement spots on the substrate^{15,26,27}. However, the long spectral acquisition times hinder the imaging of large areas in high resolution in short time, for example to study the distribution of hot spots. Therefore, the characterisation of SERS substrates suffers from the lack of a respective analytical method allowing such rapid and extensive high-resolution imaging.

Reliability and outcome of SERS experiments not only depends of the type of SERS substrate, but is also highly dependent of the actual SERS measurement procedure. For example, the reproducibility of SERS signals can be highly dependent of the size of the laser spot. Sampling errors or undersampling occurs when the size of the analysed area is below that needed to reliably represent the composition of the sample²⁸. Heterogeneous SERS substrates therefore require an illumination with large laser spot sizes to obtain reliable results. Such technical requirements are however not feasible for every Raman system, *e.g.* for an optical microscope optimized for small laser spot sizes. Alternatively, averaging could be achieved by measuring several spots on a SERS substrate. Still, sometimes such highly averaged signals of not exactly defined origin are not wanted, *e.g.* for single molecular SERS applications requiring spectral acquisition at single hot spots. Finding single hot spots on a heterogeneous substrate based on a trial-and-error procedure can be very time consuming due to an often low abundance of hot spots¹⁰. Therefore, it is not only crucial to characterise the substrates (especially with regard to hot spot localisation) but also utilize this characterisation for spatial guidance of the actual SERS measurements.

Another important aspect in SERS spectroscopy is the SERS continuum background (SERS-BG). Since the beginning of SERS research the SERS-BG is a known phenomenon, which is always generated in conjunction with the SERS effect²⁹ but mostly ignored and simply eliminated by baseline fitting³⁰. The origin of the SERS-BG is still under debate and is discussed to arise from several contributions^{29,31–39}. Irrespective of its detailed nature and like SERS itself, the SERS-BG is considered to be a localised surface plasmon resonance (LSPR)-enhanced process originating from the nanostructures of the SERS substrate^{40,41}. Controversial is the role of the analyte for the SERS-BG generation^{38,39,42}. One remarkable observation is that the signal intensity of the SERS-BG correlates with the signal intensity of the analyte^{39,43–45}. Moore et al.⁴³ revealed a relationship of analyte signals and SERS-BG signals of Rhodamine 6G enhanced by colloidal silver via 2D correlation analysis in dependence of the Raman shift. Mahaian et al.³⁹ showed that the relation between the SERS-BG maximum signal intensity and

analyte signal intensity is dependent of the SERS substrate plasmon properties, the type of molecule as well as the analyte coverage. The group of Heike Arnolds^{44,45} found a linear relationship between various vibrational signals of 4-mercaptopyridine adsorbed on a electrochemically roughened gold surface and the SERS-BG signal at 915 cm^{-1} and used this for normalisation purposes. Imaging of the SERS-BG was already applied to investigate halide treatment of immobilised silver nanoparticles by exploiting SERS-BG signals over a spectral range of 40 nm ⁴⁶, to examine the origin of the SERS-BG in a silver nanostructured film by analysing isolated spectral intervals⁴⁰ and mapping of plasmonic nanoaggregates⁴⁷ by using stage-scanning^{40,47} or wide-field illumination⁴⁶ and a CCD camera.

In this paper we introduce imaging of the SERS-BG integral under a SERS spectrum as a versatile tool for characterizing a SERS substrate as well as for improving the SERS detection procedure towards a higher reproducibility and reliability in hot spot-based high performance SERS experiments. In contrast to the earlier studies, we evaluate the SERS-BG images obtained by recording the Stokes-shifted light without spectral resolution. We use a confocal laser-scanning microscope enabling fast imaging with submicrometre resolution. Our focus is on the analytical capabilities of SERS-BG imaging and its relation to SERS enhancement. Furthermore, we show the relationship between the integrated SERS-BG under a SERS spectrum and individual Raman signal intensities of an analyte.

Based on this relationship we introduce a new SERS-BG imaging assisted SERS measurement procedure and compare it to the conventional trial-and-error SERS measurement procedure. The applicability of the SERS-BG image to obtain strongly enhanced SERS spectral information is proven by a pixel-wise acquisition of spectra at hot spots on the SERS substrate. We also show that hot spots can be evaluated for their quality of Raman signal enhancement by simultaneously detecting multiple SERS-BG imaging channels. The information obtained by the SERS-BG imaging method are correlated to additionally acquired reflection and transmission images and to the substrates' micro- and nanostructure revealed by SEM imaging. Furthermore, based on our SERS-BG imaging method we employ Monte-Carlo simulations to estimate the sampling error for randomly positioned SERS measurements with different laser spot sizes.

Results

The relationship between Raman signal intensity, SERS-BG signal intensity and the SERS-BG integral $\int I_{BG}$. For our experiments we utilised a commercial SERS substrate called Mato (Integrated Optics), which was covered with a $100\text{ }\mu\text{molar}$ ATP solution. As the overall integral of a SERS spectrum is dominated by the SERS-BG I_{BG} and only a negligible contribution is due to the narrow Raman signals, we refer in the following to the overall integral SERS spectrum as summed SERS-BG signal $\int I_{BG}$.

In Fig. 1a SERS spectra of different enhancement are shown. The intensities of the three most intense Raman signals of ATP are plotted against $\int I_{BG}$ for a total of 504 spectra. The signals originate from the adenine ring breathing vibration at 731 cm^{-1} , the PO_3^{2-} -stretching vibration at 1006 cm^{-1} and the C5-N7-stretching vibration of the adenine ring at 1334 cm^{-1} (for detailed spectral assignment see Figure S1 and Table S1). We observe strong linear relationships with high coefficients of determination (R^2) of 0.94, 0.94 and 0.99, respectively. However, at high intensities spectra tend to deviate from the linear model, most noticeably for the signal at

Loading [MathJax]/jax/output/CommonHTML/fonts/TeX/fontdata.js -wise linear models of the SERS spectra signal

intensities vs I_{BG} (Fig. S2) reveals the influence of the Raman signals. At positions of Raman signals from ATP the R^2 values decrease in correspondence to the analyte signals and follow the band shape, proving that the decreased linear relationship is indeed due to variations of the pronounced Raman signals. At positions away from the Raman signals, the intensity originates only from SERS-BG and correlates highly with I_{BG} .

We therefore separated the spectral information into the narrow Raman signals and an underlying smooth baseline by an asymmetric least squares baseline fitting. Since the baseline is assumed to be mainly due to the SERS-BG signal, we use it in this work as an estimation for the SERS-BG. As expected, the correlation between the SERS-BG and I_{BG} is very high (Fig. 1b). These results show that I_{BG} is a very good predictor for the intensity of SERS-BG signals in a SERS spectrum at individual relative wavenumbers.

However, much more relevant in the context of the SERS-BG imaging method introduced here is the relationship between I_{BG} and the intensity of the Raman signals, which both are LSPR modulated processes. For the Raman signals at 731 cm^{-1} and (to a lesser extend) at 1006 cm^{-1} the determined values differ from the linear model fit of signal intensity vs I_{BG} . This might originate from slightly different signal generation processes for SERS and SERS-BG (see introduction) or the analyte/substrate interaction. While both the SERS and SERS-BG signal intensities highly depend on the plasmonic properties of the hot spots (*e.g.* due to size and shape of the nanostructure), the effective number of analyte molecules and their orientation within the hot spots might have a more pronounced impact just on the SERS signal. Therefore, a high correlation of intense SERS signals with I_{BG} is not imperative. And indeed, the correlation of the Raman signals at 731 cm^{-1} and 1006 cm^{-1} with I_{BG} is relatively low (Fig. 1c). Nevertheless, it is still high enough to enable the differentiation of hot spot regions with high Raman signal enhancement from regions of low Raman signal enhancement by utilizing I_{BG} . The big advantage of using I_{BG} instead of a single Raman signal is its higher signal intensity by a factor of $\sim 10^3$. This allows an easy transfer to fast imaging processes by detecting I_{BG} as an integrated signal intensity along the whole SERS spectrum. This approach forms the basis for our proposed SERS-BG imaging based hot spot localisation method.

Principle of SERS-BG based SERS-Analysis. Finding the hot spots on a SERS substrate is usually difficult, because they are typically very rare and occupy just a fraction (less than 1%) of the surface¹⁰. Additionally, for high signal enhancement it is crucial to measure at the exact hot spot positions, not just in the close vicinity. For example, all 504 Raman spectra acquired in our study were taken directly at or in the vicinity of hot spots, but only 3% of them exhibited strong enhancement. Conventional SERS experiments (schematically depicted in Fig. 2a), where a laser spot is randomly focused on different positions of the SERS substrate surface until a position of high signal enhancement is found, are therefore quite challenging and time consuming procedures. Moreover, due to the rareness of hot spots, there is a high probability not to find any of the “hottest” hot spots and thus to not fully exploit the signal enhancement capabilities of the SERS substrate. This results last but not least in a decreased reproducibility and reliability. A procedure often applied to circumvent this problem, especially when dealing with heterogeneous substrates, is to use objectives with a low numerical aperture. This approach allows to focus on a large area of the substrate and thus obtain an averaged, more reproducible SERS signal and a higher probability to hit a hot spot, but it reduces the total signal intensity due to the decreased collection efficiency of low NA objectives.

By contrast, our SERS-BG imaging based method (schematically depicted in Fig. 2b) aims to acquire SERS spectra only of regions of highest signal enhancement with high spatial resolution. This is achieved by laser-scanning the red-shifted light emission I_{img} of the SERS substrate using fast and sensitive HyD detectors (HYbrid Detectors of photomultiplier tubes and avalanche diodes) before the actual SERS spectral acquisition. The optical window for detection of the emitted light is set to the wavelength range of the Raman signals and thus should collect the same spectral range as \bar{I}_{BG} . As shown in the previous section, this should allow to localise hot spots by a high intensity of I_{img} . As hot spots result from structures smaller than the wavelength of the incident light, they appear as a diffraction-limited spot in these images. Using an objective of high numerical aperture allows to localise these spots with high precision. The SERS measurement is subsequently performed by positioning the laser focus at the centre of highest intensity of these usually round-shaped spots and wavelength-dispersed detection of the Raman scattered light. This should distinctly increase the chance to obtain a SERS signal of high intensity compared to the random procedure. Thanks to the high speed of the imaging method also large areas of the SERS substrate can be measured in short time and the area can be further increased by stitching images. This significantly enhances the chance to localise several hot spots or – at best – the ‘hottest’ hot spots on the substrate.

SERS-BG based hot spot localisation and differentiation. To validate that a SERS-BG measurement images real hot spots applicable for enhancing Raman signals, we spectrally investigated the two hot spots with highest intensity of I_{img} pixel-wise after SERS-BG imaging (Fig. 3a). They both show a gradual increase of I_{img} towards the centre of the hot spot, even reaching the detector limit there (Fig. 3b and c, top). The intensities of the spectral signals (shown below the enlarged SERS-BG image) increase towards the centre of the hot spots in correspondence to I_{img} . For hot spot #1 we observe enhancement of ATP signals at 731 cm^{-1} , 1006 cm^{-1} and 1334 cm^{-1} (Fig. 3b) while for hot spot #2 strong signals are due to carbonisation apparent by the so-called D- and G-band of amorphous carbon (AC) at 1313 cm^{-1} and 1592 cm^{-1} , respectively¹¹⁻¹⁴ (Fig. 3c). Such carbonisation is a commonly observed phenomenon in SERS experiments and is most often attributed to contaminations^{12,13} or due to photophysical reactions of the analyte¹³. For quantitative evaluation we integrated the intensity data of the whole spectrum, the ATP signal at 731 cm^{-1} and the G-band at 1592 cm^{-1} to obtain \bar{I}_{BG} , \bar{I}_{ATP} and \bar{I}_{AC} , respectively (Fig. S3). The integrals, as the spectral signals, increase towards the centre of the hot spots (Fig. 3b and c bottom).

Comparison of the integration results also reveals the correlation between I_{img} , \bar{I}_{BG} and the spectral signal of ATP or AC, respectively (Fig. S4). In hot spot #1 the profile of ATP enhancement matches with \bar{I}_{BG} ($R^2 = 0.97$) as well as with the pixel intensities I_{img} obtained from the SERS-BG image ($R^2 = 0.93$). The integrated ATP signal increases from $0.1 \cdot 10^4$ at the edges of the hot spot to $3.4 \cdot 10^4$ in the centre, corresponding to an additional signal enhancement factor of 34.

In hot spot #2 we observe a similar correlation of the integrated AC band at 1592 cm^{-1} , \bar{I}_{BG} and the SERS-BG pixel intensities I_{img} . However, a linear relationship is only found between \bar{I}_{AC} and \bar{I}_{BG} . This is mainly due to saturation of the HyD detector at the three central pixels, which prevents a correlation of I_{img} with \bar{I}_{AC} or \bar{I}_{BG} (Fig. S4). The saturation of the detector is most likely caused by surface-enhanced resonance Raman-scattering of amorphous carbon species leading to an enormous signal enhancement¹³. This also results in a four times

Loading [MathJax]/jax/output/CommonHTML/fonts/TeX/fontdata.js ed to the ATP-enhancing hot spot #1.

To differentiate between the desired ATP signal enhancing hot spots and the unwanted AC-enhancing hot spots we applied a multimodal SERS-BG imaging approach. In addition to SERS-BG imaging in the full range from 640–720 nm we also performed SERS-BG imaging restricted to the spectral region of the intense AC D- and G-band from 680–720 nm (SERS-BG-AC). This method assesses rough variations of the spectral shape. Figure 4 exemplarily compares the resulting SERS-BG images for two hot spots (#3 and #4). Hot spot #3 shows a higher intensity in the SERS-BG channel (green) compared to the SERS-BG-AC channel (red), indicating that the main spectral intensity is found in the range of 640–680 nm. Hot spot #4 shows similar intensities in both channels, hinting towards high signal intensities in the AC signal region. Spectral acquisition reveals that the increased intensities in the SERS-BG-AC channel of hot spot #4 are due to the AC bands. In contrast the spectrum in hot spot #3 shows mostly ATP signals.

Our observations show that the diffraction-limited spots of highest SERS-BG intensity I_{img} on the SERS substrate found by SERS-BG imaging are indeed real hot spots and allow collection of well-enhanced SERS spectra. The exact position of the hot spot is (as expected) at the centre of the diffraction-limited spot, where SERS-BG pixel intensity as well as the intensity of spectral bands in the SERS spectrum are highest in our experiments. This proves, that the pixel intensities I_{img} of SERS-BG imaging assess the sum of the signal intensities analogous to $\int I_{\text{BG}}$ from SERS spectra, which correlate to the analyte signal intensities (see above). The SERS-BG pixel intensity profile thus follows the signal enhancement of the SERS-BG as well as of the analyte signals and is hence well suited for hot spot localisation. By using a multimodal SERS-BG imaging approach we are furthermore able to easily discriminate between hot spots enabling the measurement of useful SERS spectra and hot spots showing unwanted carbonisation effects.

Multimodal SERS-BG based SERS substrate characterisation. In order to perform more extensive optical characterisation of the SERS substrate we combined SERS-BG imaging with reflection and transmission imaging of the incident light. Additional micro- and nanostructure imaging by SEM yielded complementary information on the surface structure of the SERS substrate.

Figure 5: **Multimodal characterisation of SERS substrate.** (a) Reflection (Ex 633 nm, Em 630–636 nm, 1% laser intensity), transmission (Ex 633 nm, Em 560–750 nm, 60% laser intensity) and SERS-background images (Ex 633 nm, Em 640–720 nm, 60% laser intensity) as well as a SEM recording from the same area. SEM imaging reveals a highly chaotic structure consisting of brighter protruding hill-like regions and darker valley-like regions, which end in hole-like structures at the centre. (b) Binarised images of (a). For the optical images features of high intensity are shown ($I > 0.4 \cdot I_{\text{max}}$). For reflection, transmission and SERS-BG image 354, 114 and 44 features are determined with an average size of 634 ± 328 nm, 938 ± 691 nm and 525 ± 255 nm, respectively. For the SEM image the hole-like structures of low intensity are shown ($I < 0.3 \cdot I_{\text{max}}$). 1753 features are present in the image with a mean size of 162 ± 105 nm. (c) Overlay of all four measurement images (top) and binarised images (bottom). (d) Correlation between the optical parameters plotted in a multimodal room spanned by reflection, transmission and SERS-BG measurements. Each circle represents one pixel on the SERS substrate. Data are normalised to I_{max} for each optical modality and color-coded according to SERS-BG intensity.

We further tried to correlate the optical properties with specific nanostructural elements determined by SEM (Fig. 5a, right). However due to the chaotic structure of the SERS substrate and its complex influence on the

generation of SERS signals a simple separation of the images into features of a specific intensity range was not sufficient to link structural elements to optical behaviour (Fig. 5c), which is in line with Bell et al.⁴.

Assessment of sampling error in conventional SERS experiments by Monte-Carlo simulations. When performing SERS experiments the measured area and measurement position have a very high influence on the uniformity and repeatability of the signal enhancement and thus on the obtained SERS spectrum itself. To estimate this influence we performed Monte-Carlo simulations on the SERS-BG image of the commercial SERS substrate. We assess the impact of the measurement area size on the uniformity of the signal and the number of hot spots within the measurement area.

For our simulations, we randomly positioned a circular mask on the SERS-BG image mimicking the conventional random SERS analysis (see also Fig. 2a; for information on handling of the image edges see Fig. S5). For the area within the mask we calculated the mean SERS-BG intensity and determined the number of hot spots present. The deviation of the mean SERS-BG intensity within the mask from that of the whole image is taken as the SERS-BG sampling error (SERS-BG SE). The number of hot spots N_{HS} is determined by counting the hot spots present within the mask area. From 1000 simulation repetitions, we calculated the average and standard deviation (SD) of both, the SERS-BG SE and N_{HS} . Simulations were performed for different sizes of the circular mask thus mimicking different laser spot sizes.

Figure 6 shows the influence of the mask size on the average SERS-BG SE and on N_{HS} . The average SERS-BG signal (red dots in Fig. 6b) is close to the average intensity of the whole image independent of the spot size and only shows minor uncorrelated fluctuations. The SDs for the 1000 repeated simulations however clearly increase with decreasing mask size reaching a maximum of 46% at a minimum mask diameter of 0.29 μm revealing a high variability of the SERS-BG signals across the investigated area. Thus large spot sizes are required for reproducible measurements. The average number of hot spots within the mask (Fig. 6d) increases with the square of the mask diameter, which is due to a linear relationship between the hot spot number and the area of the mask and approaches zero at small spot sizes. This emphasises the importance of the chosen laser focus size when performing a SERS measurement in the random way described above. An objective with high numerical aperture of 1.2 for example theoretically creates a laser spot size of approximately 0.64 μm in diameter at 633 nm resulting in a SD of around 39% and a number of detected hot spots close to zero and thus is completely unsuitable for reproducible SERS measurements. Applying an objective of lower numerical aperture of 0.3 leads to a theoretical laser spot size of 2.57 μm in diameter, which almost halves the SD to around 20%. The probability to catch at least one hot spot (Figure S6a) is just around 2.3% – only in 23 out of the 1000 simulations a hot spot is assessed. Therefore, even an objective of low numerical aperture is not very suitable. Reproducible and reliable measurements are only possible for very large measurement spot sizes. This is also mentioned by the manufacturer of the substrate, who recommends a laser spot size of at least 20 μm ⁴⁸. From our simulations this would result in a SD of around 9% for the SERS-BG SE and a mean hot spot number of 1.3 ± 1.1 . This allows to obtain a SERS signal from at least one or two hot spots in 78% or 37% of the measurements, respectively (Figure S6a). However, as already mentioned by Crawford et al.²⁸ increasing the laser spot size above the objective-defined size requires specific technical equipment to widen the laser spot and concomitantly requires an increase in the laser power, which is not possible in all commercially available Raman spectrometers. Also, when using objectives with lower numerical aperture the collection efficiency of the scattered light is

decreased, thus annihilating in part the SERS enhancement of the signals. Therefore, this approach would not be the method of choice for many applications.

An alternative approach to increase the reliability of the measurement is to increase the number of measurements in an experiment, *i.e.* performing multiple measurements at different positions. This allows to increase the sampled area without changing the laser spot size as the sampled area sums up with each additional measurement, assuming the selected positions do not overlap. Using the hypothetical 0.3 NA objective for example requires 60 randomly positioned measurements to cover the same sample area as with a laser spot of 20 μm in diameter. However, as mentioned above the probability to obtain an average signal of at least two hot spots (*e.g.* for more reproducible quantitative measurements) then is still quite low. At a laser spot size of 40 μm in diameter one measurement assesses an average hot spot number of 5.1 ± 2.2 and a probability of almost 100% to hit at least two hot spots. Covering an equivalent area with this 0.3 NA objective would require 242 repeat measurements. These numbers impressively highlight that without technical widening of the laser spot the random procedure requires very time consuming experiments with a large number of repetitions to obtain reliable averaged SERS signals. By contrast, our SERS-BG based imaging method is far less time consuming while simultaneously allowing for targeted and thus reliable hot spot measurements with objectives of any NA.

The advantages of our method over the random procedure have even more impact when an exactly defined number of hot spot is of interest. From our Monte-Carlo simulations we estimate that in a random procedure the maximum probabilities to obtain exactly 1 to 5 hot spots would be found at 19 μm , 25 μm , 34 μm , 37 μm and 41 μm laser spot diameter with probabilities of 42%, 38%, 24%, 21% and 17%, respectively (Fig. 6b). Due to the high SERS substrate heterogeneity precise SERS analytics on a defined number of hot spots is hence not achievable by the standard random procedure. Also, for some experiments it may be useful to not have averaged signals, *e.g.* for single molecule SERS measurements, which are ideally based on just a single hot spot. Our SERS-BG based imaging method provides a suitable solution for both tasks. Upon imaging the substrate and localising the hot spots, suitable measurement positions can be chosen that provide exactly the desired number of hot spots.

Discussion

The introduced SERS-BG imaging based measurement procedure is an alternative approach towards reproducible and reliable SERS experiments. Using the integrated SERS-BG signals as surrogate parameter we achieve extremely short acquisition times per pixel and hence fast measurements. By rapid scanning of the SERS substrate and registering only the integrated SERS-BG signals, we can quickly and exactly image large areas and determine the number and positions of hot spots on the surface with high resolution despite their size being below the diffraction limit. Splitting the SERS-BG signals into several channels further allows to distinguish between hot spots that enhance the analyte signals and carbonisation hot spots. These feats enable the acquisition of maximally enhanced SERS spectra of the analyte specifically from hot spots selected in this way. By recording spectra at several of these hot spots and averaging the signals a sensitive as well as reproducible SERS analysis could be achieved. This should facilitate more reproducible, reliable and automatable measurements especially when dealing with highly heterogeneous SERS substrates like the commercial one investigated here. Due to the fast and precise hot spot localisation our method is especially valuable for hot spot

The two-step procedure can be further simplified by automatically setting the laser to the positions of highest SERS-BG, resulting in a more reliable, fast and user-friendly high-performance SERS procedure. Using this method in a confocal modus also allows to obtain 3D SERS-BG images with a high resolution in z direction, which enables to find the optimal positions of the SERS measurement with respect to all three spatial dimensions on the SERS substrate.

Based on our Monte-Carlo-simulations, heterogeneous SERS substrates require either illumination with large laser spots or a high number of repeat measurements to get a reliable SERS analysis in a conventional measurement procedure. However, large laser spot sizes require specific technical equipment and are at odds with usual imaging or small focus Raman systems. Our SERS-BG imaging procedure is a good alternative, as it requires exactly the components more common in research or imaging applications. We use an objective of high numerical aperture to enable imaging and spectral acquisition with high resolution. Simultaneously, we are less dependent on high laser powers due to the strong focusing of the laser.

In conclusion the introduced SERS-BG imaging method puts the mostly ignored SERS-BG signals to good use and may help to further the applicability of SERS as a more reliable routine analytical method.

Materials And Methods

Chemicals and SERS substrates. The SERS substrate “Mato” by Integrated Optics was purchased from Mountain Photonics GmbH (Landsberg am Lech, Germany). Adenosine 5'-triphosphate disodium salt hydrate (ATP, $\geq 99\%$) and $MgCl_2$ ($\geq 98\%$) were obtained from Sigma Aldrich (Taufkirchen, Germany).

Tris(hydroxymethyl)aminomethane (TRIS, $\geq 99\%$) was purchased from Carl Roth (Karlsruhe, Germany), NaCl ($\geq 99.5\%$) from Merck (Darmstadt, Germany).

TRIS buffer was prepared from TRIS (20 mM), NaCl (150 mM) and $MgCl_2$ (10 mM) and adjusted to pH 8.0 with HCl. For analyte adsorption on the SERS substrate an aliquot of 500 μ L ATP (100 μ M) in TRIS buffer was deposited with a pipet onto the centre of the substrate. After 10 minutes the drop was removed carefully without direct contact to the nanostructured substrate and the remaining solution was allowed to dry. The prepared substrate was deposited between two cover slips (Menzel glasses 25 \times 25 mm, #1, VWR, Darmstadt, Germany) and fixed with a self-made sample holder.

SERS-BG imaging and spectral acquisition. Measurements were performed with a modified Leica TCS SP8 CARS (Leica Microsystems CMS GmbH, Wetzlar, Germany). SERS-BG images of the SERS substrate were obtained in a confocal setup with 633 nm excitation (He-Ne Laser, 60% of maximum laser intensity) using a 63x water immersion objective (Leica HC PL APO 63x/1.20 W motCorr CS2). Spectrum generation and emission (Em) band separation were achieved by combining a prism with cascade-like movable mirrors and recording with a HyD detector in EPI-direction (Em 640–720 nm, 73.8 μ m physical length, 512 \times 512 pixel, scan speed 10 Hz, zoom 2.5)⁴⁹. The HyD detector was executed in a photon-counting mode allowing single photon measurements. Auto-Focus control was used for a stabilisation of the image position. Image intensities I_{img} were recorded as 8 bit integers from 0–255. Spectrally separated SERS-BG images were obtained in the same way by using two HyD detectors at the same time (Em 640–675 nm and Em 680–720 nm). Transmission images were recorded simultaneously with the SERS-BG images using a PMT in forward position in a non-confocal setup (Em 560–750 nm). Reflection images were obtained with a PMT in EPI direction (Em 630–636 nm) at low laser intensity

(1%) and by using a RT 15/85 beam splitter. Laser light was cleaned up by a laser line filter before reaching the sample. The laser power was approximately 1.8 mW and 0.03 mW at the sample for transmission and reflection imaging, respectively.

SERS spectra were acquired with the same optical setup by using the “bleach point” modus in the Leica software, enabling point-wise laser illumination (Ex 633 nm, 20% of maximum laser intensity). The laser power was approximately 0.6 mW at the sample, the acquisition time was 10 s. Pixel-by-pixel spectra recording was performed manually by moving the “bleach point”-cursor from pixel to pixel in the previously measured SERS-BG images (pixel size 144 nm). Spectra were recorded with a spectrograph IsoPlane SCT-320 (1200 lines/mm centred on 1200 cm⁻¹) and a Pixis 100B CCD camera by Princeton Instruments (Krailling, Germany) connected with the light outlet of the Leica detector system by an optical fibre (multimode, Ø 550 µm, 0.22 NA, Thorlabs, Bergkirchen, Germany). For correlation analysis of the spectral data with the image data, imaging was performed prior to the pixel-wise acquisition of spectra along a line of interest. This procedure was repeated at least three times in order to determine average images and average spectral data.

Data processing. Data preprocessing and evaluation was performed in Matlab R2015a.

Raman signals were separated from SERS-BG signals by Asymmetric Least Squares Smoothing⁵⁰ followed by Savitzky-Golay filtering. Integrated SERS-BG intensity \bar{I}_{BG} of the spectral data was determined by trapezoidal numerical integration along the whole spectrum using the ‘trapz’ function. The area of the ATP signal at around 731 cm⁻¹ (\bar{I}_{ATP}) and the area of the carbon G-band around 1592 cm⁻¹ (\bar{I}_{AC}) were determined by linear baseline fitting from 721 cm⁻¹ to 741 cm⁻¹ for the ATP signal and from 1513 cm⁻¹ to 1659 cm⁻¹ for the AC signal using Savitzky-Golay filtered spectra, respectively, followed by trapezoidal numerical integration of the respective wavenumber region (see also Fig S3). Correlation analysis of single signals of the spectra with \bar{I}_{BG} was performed with a dataset excluding the AC enhanced spectra (Fig S3, spectra following the correlation function shown in red).

For the Monte-Carlo simulations the uniformity of the signals on a SERS-BG image was determined by randomly positioning circular masks of specific size (0.29–43.25 µm diameter) on the image. As measure of accuracy we determined the sampling error (SE) as the deviation of the average SERS-BG signal intensity within the circular mask \bar{I}_{mask} from the average SERS-BG signal intensity of the whole image \bar{I}_{Img} , which is assumed to be the true value, using the formula

$$SE = (\bar{I}_{mask} - \bar{I}_{Img}) \cdot \frac{100}{\bar{I}_{Img}} [\%]$$

We repeated the Monte-Carlo simulation experiments for $N_{sim} = 1000$ runs to obtain statistically meaningful averaged sampling error values

$$\bar{SE} = \frac{1}{N_{sim}} \sum_{N_{sim}} SE$$

A standard deviation s_{sim} was determined accounting for the simulation-to-simulation variability

$$s_{sim} = \sqrt{\frac{1}{N_{sim} - 1} \sum_{N_{sim}} \left(SE - \bar{SE} \right)^2}$$

Hot spots were defined as features with intensities $> 0.4 \cdot I_{max}$ and a minimum of 4 connected pixels. The SERS-BG image was binarised using this threshold value resulting in a pixel value of 1 for hot spots and 0 for hot spot free regions. The hot spots localised within the mask area were counted to determine N_{HS} . The average number of hot spots \bar{N}_{HS} was calculated by

$$\bar{N}_{HS} = \frac{1}{N_{sim}} \sum_{N_{sim}} N_{HS}$$

The standard deviation $s_{HS, sim}$ was calculated in the same way as s_{sim} accounting for simulation-to-simulation variabilities of the number of hot spots within the mask area.

Scanning electron microscope (SEM) images were recorded on a Quanta 200 F (FEI, OR, USA) under high vacuum mode with 10 kV accelerating voltage. Registration of SEM and optical images was performed manually in Adobe Photoshop CC 2018.

Code availability. All the codes are available from the authors.

Data availability. All the data are available from the authors.

Supplementary information accompanies the manuscript in a single PDF document.

Declarations

Conflict of interests

The authors declare that they have no conflict of interests.

Author contributions statement

P.E. and E.F. designed the project. P.E. performed experiments, simulations and data processing. P.E. wrote the first draft. All authors evaluated the data, discussed the results and reviewed the manuscript.

Acknowledgement

This study was supported by the Ministerium für Innovation, Wissenschaft und Forschung des Landes Nordrhein-Westfalen, dem Regierenden Bürgermeister von Berlin - inkl. Wissenschaft und Forschung, und dem Bundesministerium für Bildung und Forschung, also in form of the Leibniz-Research-Cluster (Förderkennzeichen: 031A360E). The authors acknowledge the support of Maria Becker (Leibniz-Institut für Analytische Wissenschaften – ISAS – e.V., Dortmund, Germany) for performing the SEM measurements.

References

1. Nie, S. & Emory, S. R. Probing Single Molecules and Single Nanoparticles by Surface-Enhanced Raman Scattering. *Science* **275**, 1102–1106 (1997).
2. Kneipp, K. *et al.* Single Molecule Detection Using Surface-Enhanced Raman Scattering (SERS). *Physical Review Letters* **78**, 1667–1670, doi:10.1103/PhysRevLett.78.1667 (1997).
3. Panneerselvam, R. *et al.* Surface-enhanced Raman spectroscopy: bottlenecks and future directions. *Chemical Communications* **54**, 10–25, doi:10.1039/C7CC05979E (2018).
4. Bell, S. E. J. *et al.* Towards Reliable and Quantitative Surface-Enhanced Raman Scattering (SERS): From Key Parameters to Good Analytical Practice. *Angewandte Chemie International Edition* **59**, 5454–5462, doi:10.1002/anie.201908154 (2020).
5. Zong, C. *et al.* Surface-enhanced Raman spectroscopy for bioanalysis: reliability and challenges. *Chemical Reviews* **118**, 4946–4980 (2018).
6. Brown, R. J. C. & Milton, M. J. T. Nanostructures and nanostructured substrates for surface-enhanced Raman scattering (SERS). *Journal of Raman Spectroscopy* **39**, 1313–1326, doi:doi:10.1002/jrs.2030 (2008).
7. Huang, J.-A., Zhao, Y., Zhu, X. & Zhang, W. Averaging effect on improving signal reproducibility of gap-based and gap-free SERS substrates based on ordered Si nanowire arrays. *RSC Advances* **7**, 5297–5305, doi:10.1039/C6RA28364K (2017).
8. Huang, Y., Chen, Y., Wang, L.-L. & Ringe, E. Small morphology variations effects on plasmonic nanoparticle dimer hotspots. *Journal of Materials Chemistry C* **6**, 9607–9614, doi:10.1039/C8TC03556C (2018).
9. Michaels, A. M., Jiang & Brus, L. Ag Nanocrystal Junctions as the Site for Surface-Enhanced Raman Scattering of Single Rhodamine 6G Molecules. *The Journal of Physical Chemistry B* **104**, 11965–11971, doi:10.1021/jp0025476 (2000).
10. Fang, Y., Seong, N.-H. & Dlott, D. D. Measurement of the distribution of site enhancements in surface-enhanced Raman scattering. *Science* **321**, 388–392 (2008).
11. Tsang, J. C., Demuth, J. E., Sanda, P. N. & Kirtley, J. R. Enhanced raman scattering from carbon layers on silver. *Chemical Physics Letters* **76**, 54–57, doi:https://doi.org/10.1016/0009-2614(80)80603-8 (1980).
12. Kudelski, A. & Pettinger, B. SERS on carbon chain segments: monitoring locally surface chemistry. *Chemical Physics Letters* **321**, 356–362, doi:https://doi.org/10.1016/S0009-2614(00)00330-4 (2000).
13. Bjerneld, E. J., Svedberg, F., Johansson, P. & Käll, M. Direct Observation of Heterogeneous Photochemistry on Aggregated Ag Nanocrystals Using Raman Spectroscopy: The Case of Photoinduced Degradation of Aromatic Amino Acids. *The Journal of Physical Chemistry A* **108**, 4187–4193, doi:10.1021/jp037004I (2004).

14. Itoh, K. *et al.* Raman Microspectroscopic Study on Polymerization and Degradation Processes of a Diacetylene Derivative at Surface Enhanced Raman Scattering Active Substrates. 2. Confocal Raman Microscopic Observation of Polydiacetylene Adsorbed on Active Sites. *The Journal of Physical Chemistry B* **109**, 271–276, doi:10.1021/jp0403644 (2005).
15. Caridad, J. M. *et al.* Hot-Volumes as Uniform and Reproducible SERS-Detection Enhancers in Weakly-Coupled Metallic Nanohelices. *Scientific Reports* **7**, 45548, doi:10.1038/srep45548
16. <https://> (2017).
17. Willets, K. A. Super-resolution imaging of SERS hot spots. *Chemical Society Reviews* **43**, 3854–3864, doi:10.1039/C3CS60334B (2014).
18. Kusch, P. *et al.* Dual-Scattering Near-Field Microscope for Correlative Nanoimaging of SERS and Electromagnetic Hotspots. *Nano Letters* **17**, 2667–2673, doi:10.1021/acs.nanolett.7b00503 (2017).
19. Dab, C., Awada, C., Merlen, A. & Ruediger, A. Near-field chemical mapping of gold nanostructures using a functionalized scanning probe. *Physical Chemistry Chemical Physics* **19**, 31063–31071 (2017).
20. Awada, C. *et al.* High resolution scanning near field mapping of enhancement on SERS substrates: comparison with photoemission electron microscopy. *Physical Chemistry Chemical Physics* **18**, 9405–9411, doi:10.1039/C5CP08015K (2016).
21. Wu, Y., Li, G. & Camden, J. P. Probing nanoparticle plasmons with electron energy loss spectroscopy. *Chemical Reviews* **118**, 2994–3031 (2017).
22. Willets, K. A., Wilson, A. J., Sundaresan, V. & Joshi, P. B. Super-resolution imaging and plasmonics. *Chemical Reviews* **117**, 7538–7582 (2017).
23. Peksa, V. *et al.* Quantitative SERS Analysis of Azorubine (E 122) in Sweet Drinks. *Anal. Chem.* **87**, 2840–2844, doi:10.1021/ac504254k (2015).
24. Pazos-Pérez, N. *et al.* Highly uniform SERS substrates formed by wrinkle-confined drying of gold colloids. *Chemical Science* **1**, 174–178 (2010).
25. Wei, H. *et al.* Improved quantitative SERS enabled by surface plasmon enhanced elastic light scattering. *Anal. Chem.* **90**, 3227–3237 (2018).
26. Cong, S. *et al.* Electrochromic semiconductors as colorimetric SERS substrates with high reproducibility and renewability. *Nature Communications* **10**, 678, doi:10.1038/s41467-019-08656-6 (2019).
27. Shi, G. C. *et al.* Dragonfly wing decorated by gold nanoislands as flexible and stable substrates for surface-enhanced Raman scattering (SERS). *Scientific Reports* **8**, 6916 (2018).
28. Tang, J., Ou, Q., Zhou, H., Qi, L. & Man, S. Seed-mediated electroless deposition of gold nanoparticles for highly uniform and efficient SERS enhancement. *Nanomaterials* **9**, 185 (2019).
29. Crawford, A. C., Skuratovsky, A. & Porter, M. D. Sampling error: Impact on the quantitative analysis of nanoparticle-based surface-enhanced Raman scattering immunoassays. *Anal. Chem.* **88**, 6515–6522 (2016).
30. Ikeda, K., Suzuki, S. & Uosaki, K. Enhancement of SERS Background through Charge Transfer Resonances on Single Crystal Gold Surfaces of Various Orientations. *Journal of the American Chemical Society* **135**, 17387–17392, doi:10.1021/ja407459t (2013).
31. Lin, K.-Q. *et al.* Plasmonic photoluminescence for recovering native chemical information from surface-

32. <https://> (2017).
33. Cai, Y.-Y. *et al.* Anti-Stokes Emission from Hot Carriers in Gold Nanorods. *Nano Letters* (2019).
34. Zhang, T. *et al.* Photoluminescence of a single complex plasmonic nanoparticle. *Scientific Reports* **4**, 3867, doi:10.1038/srep03867 (2014).
35. Ngoc, L. L. T., Wiedemair, J., van den Berg, A. & Carlen, E. T. Plasmon-modulated photoluminescence from gold nanostructures and its dependence on plasmon resonance, excitation energy, and band structure. *Optics Express* **23**, 5547–5564 (2015).
36. Cai, Y.-Y. *et al.* Photoluminescence of gold nanorods: Purcell effect enhanced emission from hot carriers. *ACS Nano* **12**, 976–985 (2018).
37. Lin, K.-Q. *et al.* Intraband hot-electron photoluminescence from single silver nanorods. *ACS Photonics* **3**, 1248–1255 (2016).
38. Hugall, J. T. & Baumberg, J. J. Demonstrating Photoluminescence from Au is Electronic Inelastic Light Scattering of a Plasmonic Metal: The Origin of SERS Backgrounds. *Nano Letters* **15**, 2600–2604, doi:10.1021/acs.nanolett.5b00146 (2015).
39. Mertens, J., Kleemann, M.-E., Chikkaraddy, R., Narang, P. & Baumberg, J. J. How Light Is Emitted by Plasmonic Metals. *Nano Letters* **17**, 2568–2574, doi:10.1021/acs.nanolett.7b00332 (2017).
40. Barnett, S. M., Harris, N. & Baumberg, J. J. Molecules in the mirror: how SERS backgrounds arise from the quantum method of images. *Physical Chemistry Chemical Physics* **16**, 6544–6549, doi:10.1039/C4CP00093E (2014).
41. Mahajan, S. *et al.* Understanding the surface-enhanced Raman spectroscopy “background”. *The Journal of Physical Chemistry C* **114**, 7242–7250 (2009).
42. Farcau, C. & Astilean, S. Evidence of a surface plasmon-mediated mechanism in the generation of the SERS background. *Chemical Communications* **47**, 3861–3863, doi:10.1039/C0CC05190J (2011).
43. Park, J.-E., Kim, J. & Nam, J.-M. Emerging plasmonic nanostructures for controlling and enhancing photoluminescence. *Chemical Science* **8**, 4696–4704 (2017).
44. Cheng, Y. *et al.* Enhanced light emission from plasmonic nanostructures by molecules. *The Journal of Physical Chemistry C* **121**, 23626–23632 (2017).
45. Moore, A. A., Jacobson, M. L., Belabas, N., Rowlen, K. L. & Jonas, D. M. 2D correlation analysis of the continuum in single molecule surface enhanced Raman spectroscopy. *Journal of the American Chemical Society* **127**, 7292–7293 (2005).
46. Aitchison, H. *et al.* Analytical SERS: general discussion. *Faraday Discussions* **205**, 561–600, doi:10.1039/C7FD90096A (2017).
47. Wattanavichean, N., Casey, E., Nichols, R. J. & Arnolds, H. Discrimination between hydrogen bonding and protonation in the spectra of a surface-enhanced Raman sensor. *Physical Chemistry Chemical Physics* **20**, 866–871 (2018).
48. Doering, W. E. & Nie, S. Single-Molecule and Single-Nanoparticle SERS: Examining the Roles of Surface Active Sites and Chemical Enhancement. *The Journal of Physical Chemistry B* **106**, 311–317, doi:10.1021/jp011730b (2002).
49. Carnegie, C. *et al.* Mapping SERS in CB: Au Plasmonic Nanoaggregates. *ACS Photonics* **4**, 2681–2686,

50. ATO ID. *Gold SERS substrate 'Mato'*, <<http://atoid.com/shop/sersgolds/>> (2019).
51. Leica Microsystems. *Leica HyD for Confocal Imaging*, <https://www.leica-microsystems.com/fileadmin/downloads/Leica%20TCS%20SP8/Brochures/Leica%20TCS%20SP8%20HyD-Brochure_EN.pdf> (2014).
52. Eilers, P. H. C. & Boelens, H. *Baseline Correction with Asymmetric Least Squares Smoothing*. (unpublished manuscript, 2005).

Figures

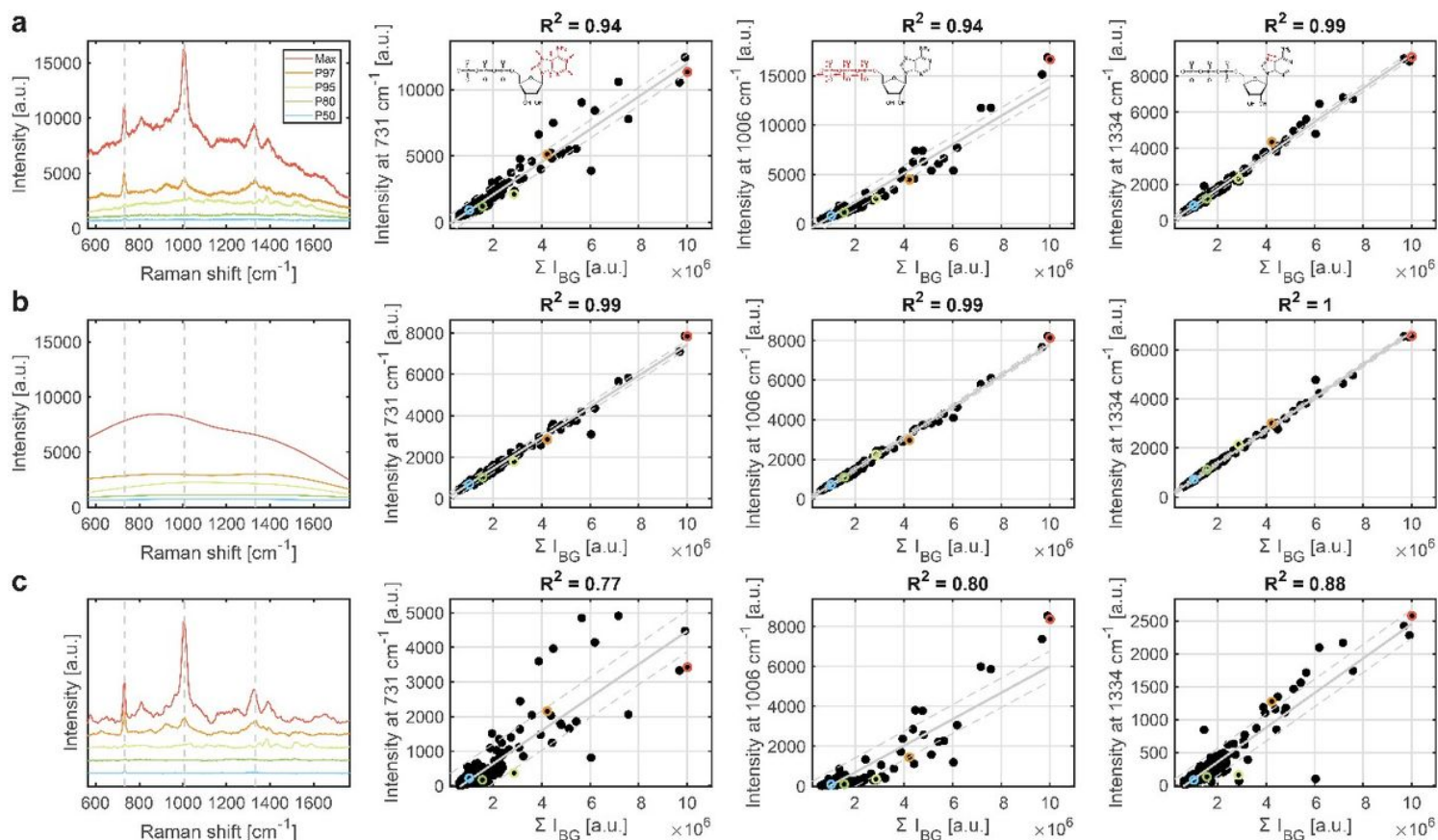


Figure 1

SERS spectra and correlation of single signals with the overall integral of the SERS spectrum (ΣI_{BG}). (a) Raw spectra of ATP and correlation of the vibrations at 731 cm^{-1} (adenine ring breathing vibration), 1006 cm^{-1} (PO32-stretching vibration) and 1334 cm^{-1} (C5-N7 stretching vibration of the adenine ring) with ΣI_{BG} . (b) SERS-BG signals derived from (a) by asymmetric least squares baseline fitting and the correlation of the resulting signal intensities at the positions from (a) with ΣI_{BG} . (c) Raman signals derived from (a) after subtracting the SERS-BG signals from (b) and the correlation of the respective signal intensities with ΣI_{BG} . From a total of 504 spectra acquired in this work, the spectra representing the percentiles 50, 80, 95, and 97 of ΣI_{BG} are shown as well as the spectrum at the maximum value of ΣI_{BG} . The linear fit is depicted by the grey line with the 95 % confidence interval marked by dashed lines. Spectra in (c) are smoothed by a Savitzky-Golay filter and shifted in intensity for better visualisation.

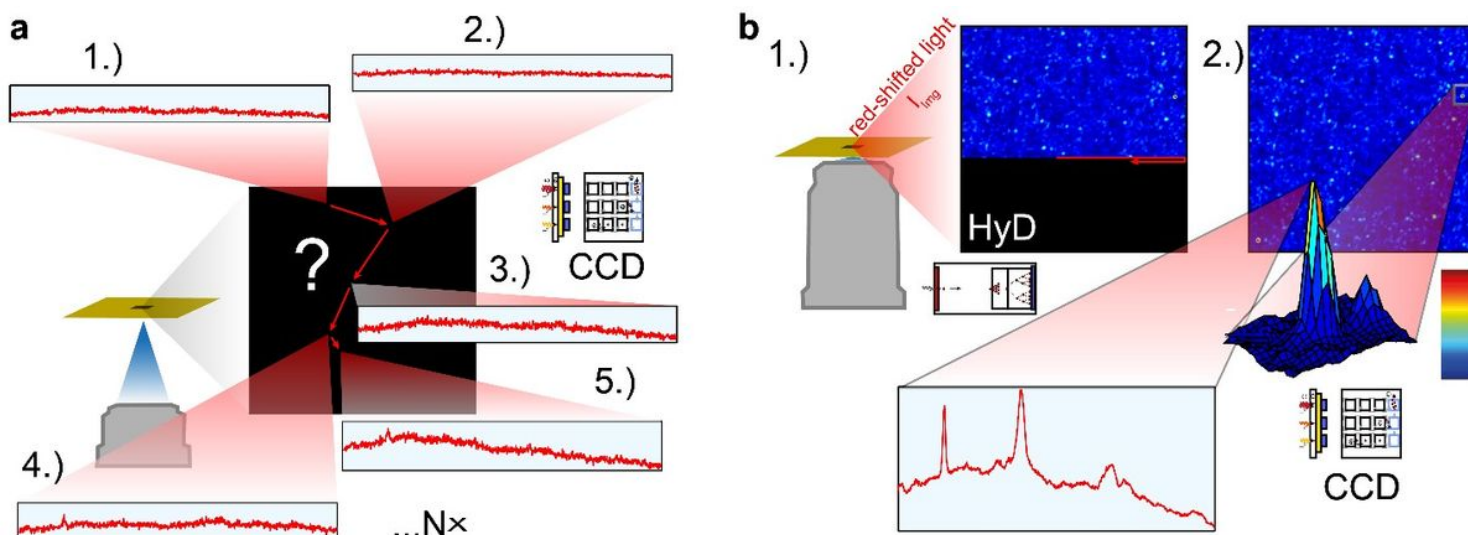


Figure 2

Schematic representation of SERS measurement procedures. (a) In a conventional SERS measurement procedure the position on the SERS substrate is randomly selected until a region of high signal enhancement is found. An objective of low NA enables to illuminate a large area and get a more averaged signal. The illustration shows five spectra recorded subsequently at different positions on the substrate acquired with a spectrograph with CCD camera. (b) For the SERS background (SERS-BG) imaging based procedure first an image of a large area of the substrate is laser-scanned and the red shifted light I_{img} is detected by a sensitive and fast HyD detector using a high NA objective. The resulting SERS-BG image visualises regions of high signal enhancement (hot spots), which are highlighted here by the bright points on the intensity heat map. In a second step the actual SERS spectra acquisition is performed only at the centre of a hot spot with the CCD spectrograph, enabling a faster and more sensitive recording of SERS spectra. An objective of high NA facilitates the localisation of the centre of a diffraction-limited hot spot area with high resolution in the first step and the recording of the enhanced Raman signals almost only from an individual hot spot area in the second step.

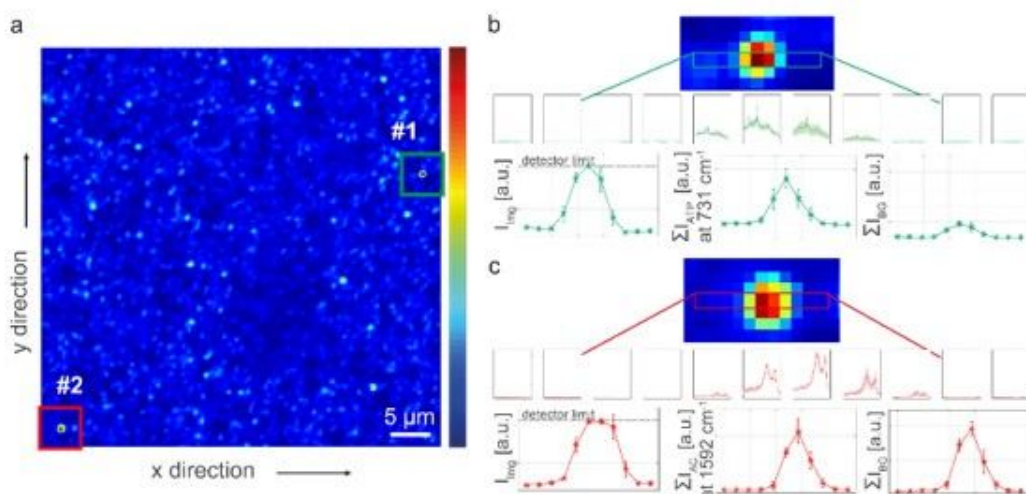


Figure 3

Result of SERS background imaging (SERS-BG). (a) SERS-BG image of a SERS substrate immersed with a 100 μM solution of ATP (Ex 633 nm, Em 640 – 720 nm). Image intensity (I_{img}) is illustrated as heat map. Two hot spots that are pixel-wise spectrally investigated along x direction are highlighted with coloured boxes with hot spot #1 shown in (b) and hot spot #2 in (c), respectively. On the right side the results of the pixel-wise spectral investigations are depicted. Top: SERS-BG image of the respective hot spot. The spectrally investigated line of pixels is framed by a box. Centre: SERS spectra from the pixels within the frame are shown as mean with standard deviation derived from three spectra per pixel. Bottom: Pixel-wise intensity of I_{img} , I_{ATP} or I_{AC} and I_{BG} (from left to right). I_{ATP} , I_{AC} and I_{BG} follow the image intensity profile in both hot spots.

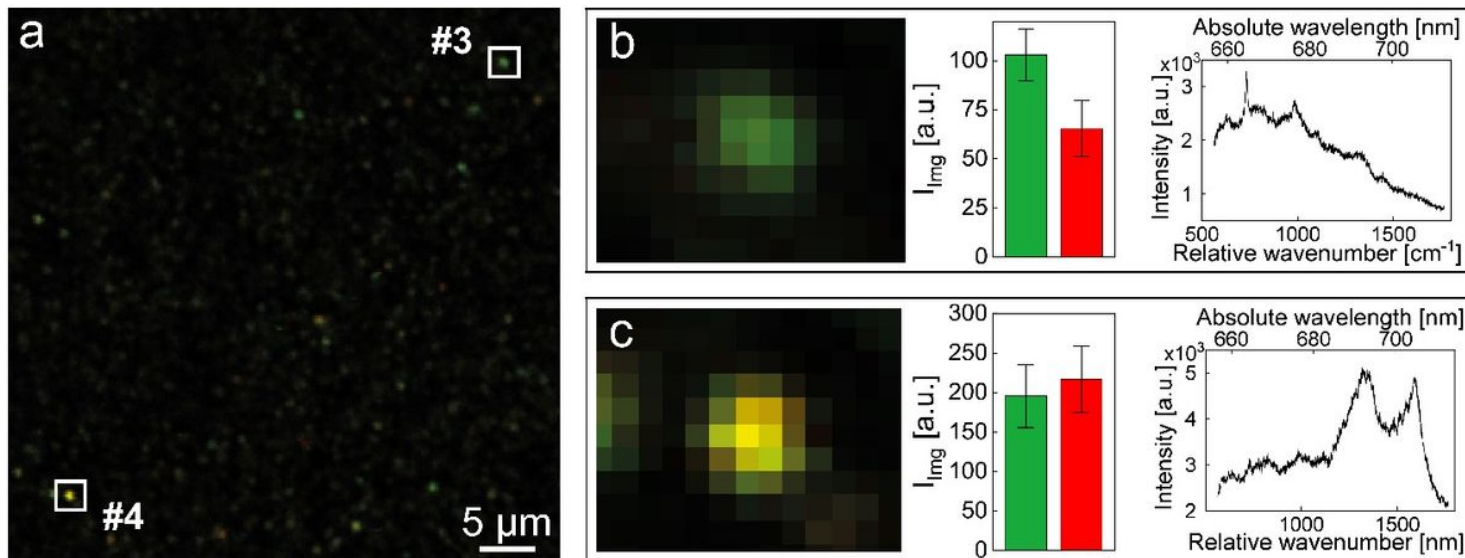


Figure 4

Differentiation of hot spots. (a) Overlay of a SERS-BG image (signals of the whole fingerprint region, 640 – 720 nm, green) with a SERS-BG AC image (signals of the range of the G- and D-band of amorphous carbon, Em 680 – 720 nm, red). High intensity in both images results in yellow colouring of the pixels. (b) Magnification of hot spot #3 from (a) (left), bar plot of the signal intensities from the SERS-BG (green) and SERS-BG AC (red) image (centre) and the SERS spectrum measured at the pixel with highest I_{img} (right). The intensity in the SERS-BG image is higher than in the SERS-BG AC image. The spectrum is dominated by ATP signals. (c) Magnification of hot spot #4 from (a) (left), bar plot of the signal intensities from the SERS-BG (green) and SERS-BG AC (red) image (centre) and the SERS spectrum measured at the pixel with highest I_{img} (right). The SERS-BG image and the SERS-BG AC image show similar intensities. The spectrum is dominated by AC signals. Measurements were performed on a Mato SERS substrate immersed with 100 μM ATP solution (Ex 633 nm). For signal intensities of the bar plots the four most intense pixels per hot spot and spectral range were evaluated from triplicate measurements.

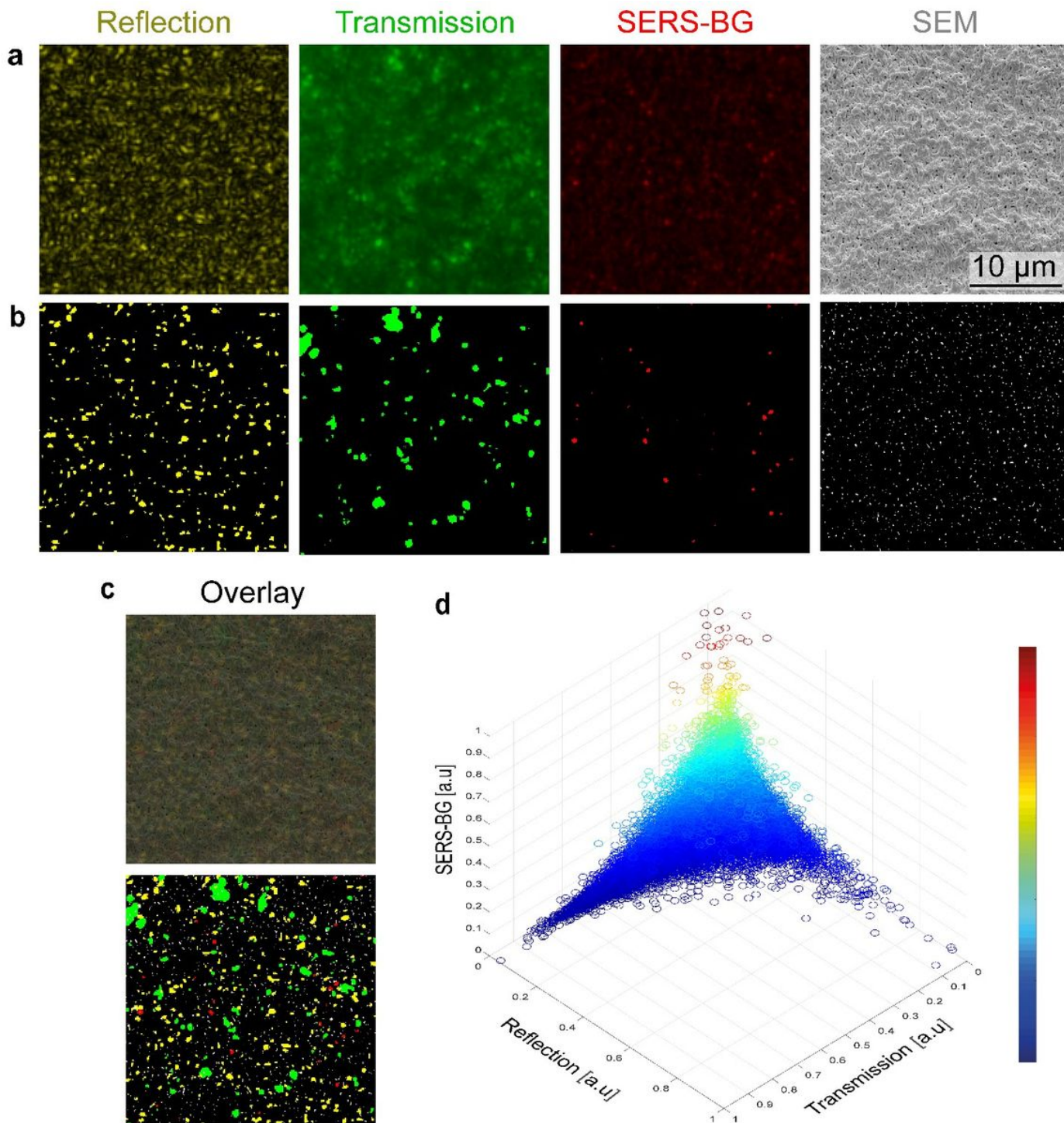


Figure 5

Multimodal characterisation of SERS substrate. (a) Reflection (Ex 633 nm, Em 630 – 636 nm, 1 % laser intensity), transmission (Ex 633 nm, Em 560– 750 nm, 60 % laser intensity) and SERS-background images (Ex 633 nm, Em 640 – 720 nm, 60 % laser intensity) as well as a SEM recording from the same area. SEM imaging reveals a highly chaotic structure consisting of brighter protruding hill-like regions and darker valley-like regions, which end in hole-like structures at the centre. (b) Binarised images of (a). For the optical images features of high intensity are shown ($I > 0.4 \cdot I_{max}$). For reflection, transmission and SERS-BG image 354, 114 and 44 features are determined with an average size of 634 ± 328 nm, 938 ± 691 nm and 525 ± 255 nm, respectively. For the SEM [Loading \[MathJax\]/jax/output/CommonHTML/fonts/TeX/fontdata.js](#) $I < 0.3 \cdot I_{max}$). 1753 features are present in the image

with a mean size of 162 ± 105 nm. (c) Overlay of all four measurement images (top) and binarised images (bottom). (d) Correlation between the optical parameters plotted in a multimodal room spanned by reflection, transmission and SERS-BG measurements. Each circle represents one pixel on the SERS substrate. Data are normalised to I_{\max} for each optical modality and color-coded according to SERS-BG intensity.

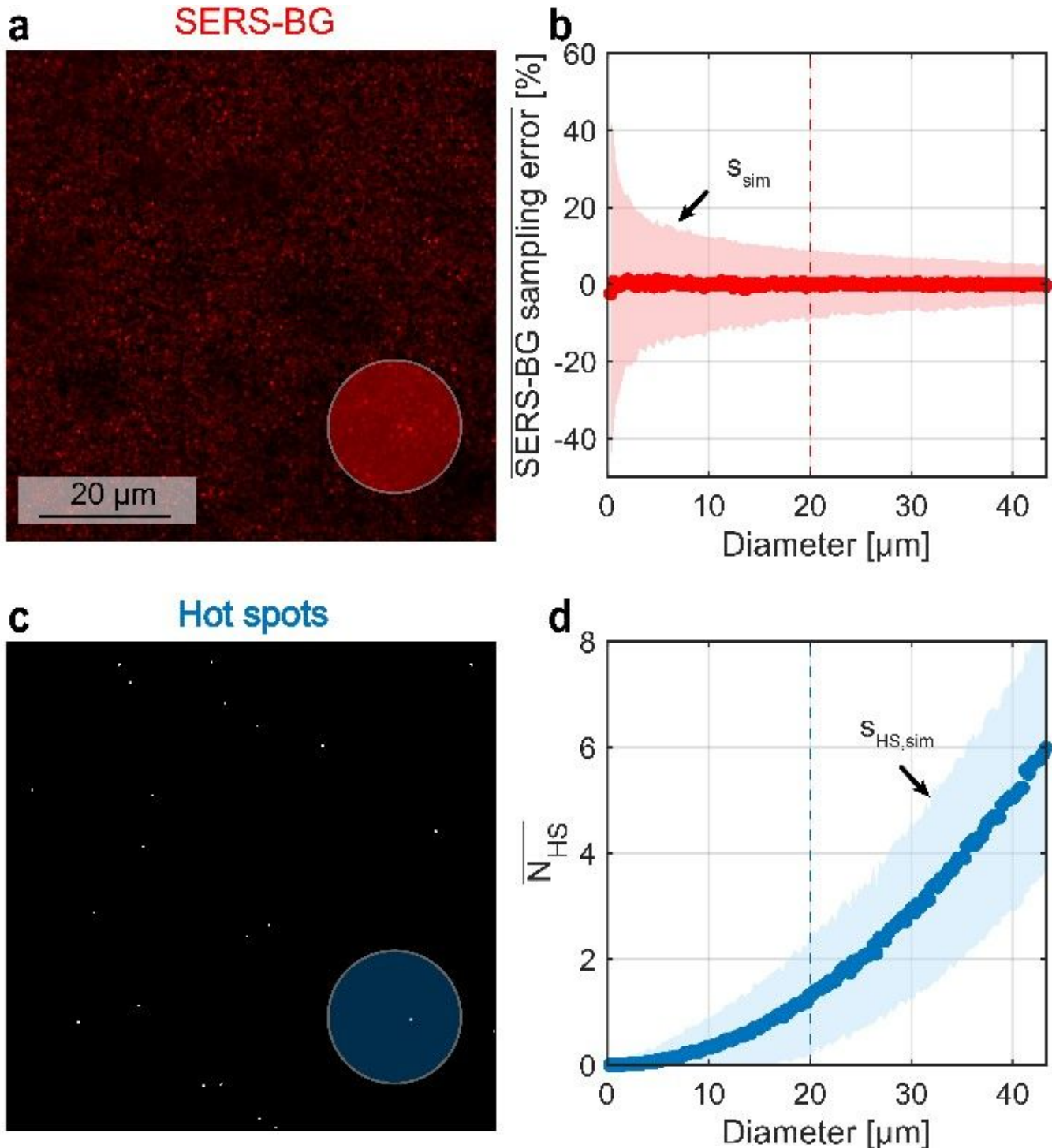


Figure 6

Results of Monte-Carlo simulations. (a) SERS-BG intensity image with exemplary circular mask representing the sampling area, (b) influence of the mask size on the SERS-BG sampling error, (c) distribution of hot spots determined by SERS-BG imaging, (d) influence of the mask size on the number of hot spots within the mask

area. All data are determined from 1000 repeat simulations per mask size and given as mean (dots) and standard deviation (shaded regions).

Supplementary Files

This is a list of supplementary files associated with this preprint. Click to download.

- [EbersbachSERSBGSI.pdf](#)